Structure determination from XAFS using high-accuracy measurements of x-ray mass attenuation coefficients of silver, 11 keV–28 keV, and development of an all-energies approach to local dynamical analysis of bond length, revealing variation of effective thermal

2015 J. Phys.: Condens. Matter 27 266301

(http://iopscience.iop.org/0953-8984/27/26/266301)

IOP Publishing Journal of Physics: Condensed Matter

J. Phys.: Condens. Matter **27** (2015) 266301 (17pp) doi:10.1088/0953-8984/27/26/266301

Structure determination from XAFS using high-accuracy measurements of x-ray mass attenuation coefficients of silver, 11 keV–28 keV, and development of an all-energies approach to local dynamical analysis of bond length, revealing variation of effective thermal contributions across the XAFS spectrum

L J Tantau[1], C T Chantler[1], J D Bourke[1], M T Islam[1], A T Payne[1], N A Rae[1] and C Q Tran[2]

[1] School of Physics, University of Melbourne, Victoria 3010, Australia
[2] Department of Physics, LaTrobe University, Victoria 3086, Australia

E-mail: chantler@physics.unimelb.edu.au

Received 26 February 2015, revised 12 May 2015
Accepted for publication 15 May 2015
Published 15 June 2015

Abstract

We use the x-ray extended range technique (XERT) to experimentally determine the mass attenuation coefficient of silver in the x-ray energy range 11 kev–28 kev including the silver K absorption edge. The results are accurate to better than 0.1%, permitting critical tests of atomic and solid state theory. This is one of the most accurate demonstrations of cross-platform accuracy in synchrotron studies thus far. We derive the mass absorption coefficients and the imaginary component of the form factor over this range. We apply conventional XAFS analytic techniques, extended to include error propagation and uncertainty, yielding bond lengths accurate to approximately 0.24% and thermal Debye–Waller parameters accurate to 30%. We then introduce the FDMX technique for accurate analysis of such data across the full XAFS spectrum, built on full-potential theory, yielding a bond length accuracy of order 0.1% and the demonstration that a single Debye parameter is inadequate and inconsistent across the XAFS range. Two effective Debye–Waller parameters are determined: a high-energy value based on the highly-correlated motion of bonded atoms ($\sigma_{DW} = 0.1413(21)$ Å), and an uncorrelated bulk value ($\sigma_{DW} = 0.1766(9)$ Å) in good agreement with that derived from (room-temperature) crystallography.

Keywords: x-ray mass attenuation coefficient, atomic form-factor, XERT, integrated column density, XAFS

(Some figures may appear in colour only in the online journal)

1. Introduction

X-ray mass attenuation coefficients $\left[\frac{\mu}{\rho}\right]$ describe fundamental absorption and scattering interactions between light and matter. These interactions are an ideal probe in many systems due to their strong surface penetration and detailed energy-dependence. Of particular interest in the relevant energy regime is x-ray absorption fine structure (XAFS), a phenomenon that is highly sensitive to molecular structure, electron density, coordination number, oxidation and ionisation states, and conformational properties of condensed matter systems [1].

In recent years concerted effort has been made to improve and develop specialised measurement and analytic techniques for XAFS due to these sensitivities. These techniques have varied widely by application, but include rapid-response stages and detectors for ultra-fast XAFS measurements [2], development of high-pressure sample cells for investigation of temperature-dependent chemical phenomena [3], optimisation of detector characteristic for noise minimisation [4], and extended-range measurement techniques for high-accuracy quantification and elimination of systemic errors [5].

The latter development is characterised by the x-ray extended range technique (XERT)—an XAS measurement approach capable of determining mass attenuation coefficients with uncertainties well below 0.1% over energy ranges spanning several keV. The XERT was developed specifically to interrogate known discrepancies between longstanding theoretical calculations, and also discrepancies between established experimental measurements. It is also designed to improve information content from XAS tabulations—a critical endeavour even in modern spectroscopy where serious questions still exist about the detailed nature of scattering and absorption processes [6].

Developments of *ab initio* solid state theories in x-ray absorption have also demanded further progress in high accuracy absolute measurements of x-ray mass attenuation coefficients focussed on the energy regime where solid state effects are dominant. The characteristic XAFS spectrum consists of complex oscillations in absorption spectrum at energies just beyond an absorption edge due to the interference of the photoelectron wave with the surrounding electron densities [7]. Recent developments in quantification of these oscillations using the Finite Difference Method for Near Edge Structure (FDMNES) [8] and the Finite Difference Method for XAFS (FDMX) [9] are of particular interest and relevance to this work, as they demonstrate the application of full-potential theory to the robust analysis of XAFS data over the entire energy spectrum. Measurements made employing the x-ray Extended Range Technique (XERT) [10] have been used recently with FDM-based approaches to extract information about electron energy loss functions and electron inelastic mean free paths (IMFPs) in solids [11, 12].

In this work we demonstrate how such a combination of investigative approaches may be further developed to interrogate detailed information regarding crystalline bond lengths, refined lattice parameters, and temperature parameters via the mean-square deviation of atomic displacements—i.e. the Debye–Waller factor σ^2_{DW}.

2. Experimental details

2.1. Beamline

Measurements were made at the Australian National Beamline Facility (ANBF) on BL 20B at the Photon Factory in Japan. X-rays from a bending magnet were monochromated by a channel-cut monolithic Si (311) crystal. Reflections from the 311 plane are desired as they naturally suppress second order harmonics, and are ideal for x-ray monochromation in the desired energy range. The beam was collimated to a 1×0.5 mm^2 cross sectional area.

The monochromatic beam passed through the high resolution powder diffractometer BigDiff, which was used to accurately determine the energy of the beam using well defined powder samples. The incident and transmitted intensities were recorded by two 5 cm ion chambers, with krypton used as the ionising gas (figure 1). The two ion chambers were connected in series in order to ensure strong positive correlation between repeated measurements [13, 14].

2.2. Samples

Six high purity silver foils were carefully chosen to ensure that for each energy, at least one absorber would satisfy Nordfors' criterion (e.g. $2 < \ln(I/I_o) < 4$) for counting statistics [15–17]. Each foil had a cross sectional area of 25×25 mm^2 with nominal thicknesses of 1 μm, 10 μm, 12.5 μm, 2×50 μm and 100 μm. Purity levels are assessed by Goodfellows, at the 99.95+% level.

3. Determining the mass attenuation coefficient

3.1. Measuring attenuation from count rates

Measurements of the incident and transmitted intensity of the x-ray beam, I_u and I_d respectively were made by recording the number of counts in each ion chamber. The counts represent the number of ionisation events in the ion chambers, providing a measure of the beam flux. In this manner the ratio of intensities between the upstream and downstream ion chambers are able to measure how many photons were removed from the beam by the absorber. Other considerations must be taken into account to achieve an accurate measure of the absorption of a sample. Measurements are made when there are no incident x-rays (dark-current) at the experimental station in order to determine the non-zero count rate in the ion chambers whilst the beam is off. The dark-current becomes very important for thick absorbers at high attenuation levels and becomes a dominant contribution to the uncertainty. Once the dark current has been measured, the ratio of intensities is then

$$I = \overline{\left(\frac{I_d - dc_d}{I_u - dc_u}\right)}, \tag{1}$$

where dc_u and dc_d are the upstream and downstream measured dark-currents. The ratio of intensities is measured as the average of repeated measurements in order to approximate the local consistency and hence the uncertainty of the measurements. Since the dark current counts vary very slowly over time, a straight

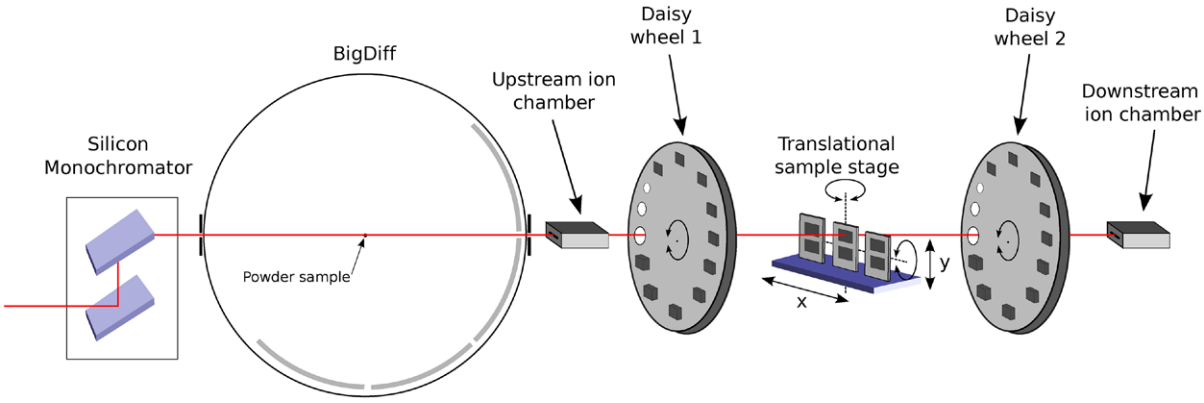

Figure 1. Schematic of the experimental layout. The collimated monochromated beam is analysed in the BigDiff diffractometer to determine the beam energy to 1–2 eV, with ion chambers providing the monitor and detector signals for the transmission experiment, daisy wheels configured to measure scattering and harmonic contributions and multiple samples to determine the thickness-independent mass attenuation coefficient.

line function is used to model the measurements with respect to time, and the uncertainty is obtained from the covariance matrix returned during the fitting procedure. The ratio of intensities is related to the mass attenuation coefficient such that

$$\left[\frac{\mu}{\rho}\right][\rho \mathrm{t}] = -\ln\left(\frac{I_s}{I_b}\right), \tag{2}$$

where $[\rho \mathrm{t}]$ is the integrated column density of the sample, $[\mu/\rho]$ is the mass attenuation coefficient, and the subscripts b and s represent a blank measurement and sample measurement respectively, correcting for air path and other beam optics. This is the relationship of the Beer–Lambert law [5].

With these additional measurements, the attenuation of each absorber can be measured free of specific beamline effects such as the ratio of counts between the detectors when no sample is in place and the non-zero count rate measured when there are no incident photons. Each measurement was made over a 0.1 s or 1 s interval and repeated six or ten times to determine the counting statistics and local reproducibility of the measurements. The uncertainty of the repeated measurements is reported here as the standard deviation of the ratio of intensities, and is added in quadrature with the uncertainty of the dark current measurements.

$$\sigma_I^2 = \sigma_{s.d}^2 + \left[\frac{\partial I}{\partial(dc_d)}\Delta_{dc_d}\right]^2 + \left[\frac{\partial I}{\partial(dc_u)}\Delta_{dc_u}\right]^2, \tag{3}$$

where Δ_{dc_d} and Δ_{dc_u} are the uncertainties in the upstream and downstream dark current readings respectively. For strong attenuators, the dark current uncertainty becomes dominant [18].

Repeated measurements with a high (positive) correlation coefficient permit the average intensity ratio to be determined from the average ratio of intensities over the repeated measurements [13, 14]. Following equations (1) and (2) the Beer–Lambert law becomes

$$\left[\frac{\mu}{\rho}\right][\rho \mathrm{t}] = -\ln\left[\left(\frac{\overline{I_d - dc_d}}{I_u - dc_d}\right)_s \Big/ \left(\frac{\overline{I_d - dc_d}}{I_u - dc_d}\right)_b\right], \tag{4}$$

and the final uncertainty in the attenuation of each foil is then the quadrature sum of the blank measurement and sample measurement,

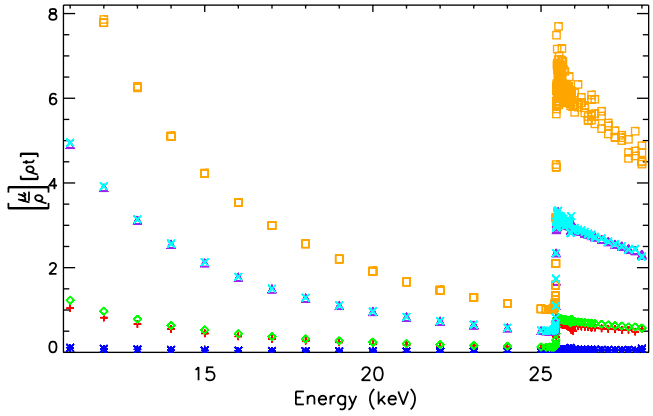

Figure 2. Measured attenuation $[\mu/\rho][\rho \mathrm{t}] = -\ln\left(\frac{I_s}{I_b}\right)$. The markers represent results obtained using foils of nominal thickness: □—100 μm, ×—50 μm, △—50 μm, ⋄—12.5 μm, +—10 μm, ∗—1 μm.

$$\sigma_{[\mu/\rho][\rho \mathrm{t}]} = \left[\left(\frac{\sigma_I}{I}\right)_b^2 + \left(\frac{\sigma_I}{I}\right)_s^2\right]^{\frac{1}{2}}. \tag{5}$$

The use of multiple foils ensures that there is at least one foil that lies within Nordfors range at each energy [15]. This is demonstrated in figure 2.

The functional form of the uncertainties in $[\mu/\rho]$ for each foil demonstrated in figure 3 gives an indication of the reliability of the foil measurements as a function of energy. The orange squares which represent the thickest foil exhibit an increasing trend of uncertainty as the energy decreases and absorption increases. There is at least one foil with measurement uncertainties less than 0.1% or 0.2% at every energy, aside from the measurements at 21 kev and measurements above 26 kev, where the lowest uncertainty is around 1%.

3.2. Sample characterization

The silver foils used in this work present as microcrystalline but highly disordered, implying that the elastic scattering will in general follow Rayleigh approximations. Hence expected

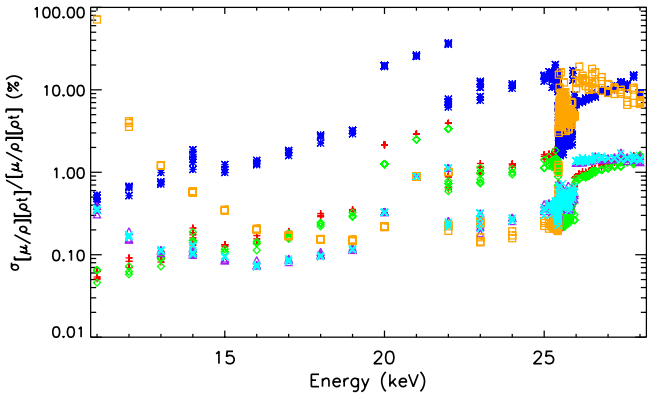

Figure 3. Percentage uncertainties of data obtained with the various foils. The markers represent results obtained using foils of nominal thickness: □—100 μm, ×—50 μm, △—50 μm, ⋄—12.5 μm, +—10 μm, ∗—1 μm.

defects and phase boundaries are an advantage in this work. Any deviation or for example local alignment of a particular foil region with coherent Bragg diffraction peaks are directly observed and corrected for in the procedure. None were observed in this experiment, implying the upper limit of that effect is at the level of the final uncertainty in precision.

The background is affected by impurities rather than the XAFS structure. However, for the absolute accuracy of our results this is important; and indeed for heavy element contamination such as gold impurities there could be impact upon the XAFS region. Typical impurity levels for these samples are 70 ppm Cu, 5 ppm Fe and Zn and 1 ppm Na and Pb [19]. The effect of these impurities on the measurements were calculated to no more than −0.007% below the edge and +0.006% above the edge, hence are insignificant. Calculations were also made regarding the possibility of an oxide layer developing on the front and back of the foils. A typical value of 30 Å [20] was used for the combination of the front and back oxide layer and the effect was calculated to be no greater that 0.0003% for the thinnest foil (most affected) at all energies.

Further details of the characterisation techniques used for our foils, including full-foil mapping and measurements of the integrated column density, are outlined in other works [21, 22]. We also provide key details for the silver measurements in the appendix A.

3.3. Final uncertainties

In this work we have identified and estimated multiple sources of uncertainty. The statistical uncertainties of each foil presented in figure 3 represent the spread of ratios calculated from the repeated measurements, and uncertainties arising from the dark current uncertainty. These values are only used to estimate the uncertainty of each measurement, so that the fitting procedure is not biased by data of lower quality.

Once all integrated column densities and various other parameters related to systematics have been fitted to the data set, the mass attenuation coefficient at each energy is then determined by taking the weighted mean of all foil and aperture conditions at each energy. The input uncertainties are the statistical uncertainty of the absorption measurements.

$$(\Delta_{[\mu/\rho]})_r = \sqrt{\frac{\sum_i w_i([\mu/\rho]_i - \overline{[\mu/\rho]})^2}{N \times \sum_i w_i}} \tag{6}$$

where $w_i = 1/\sigma_i^2$, σ is the estimated uncertainty in the attenuation measurements and N is the total number of measurements made which related to the weighted mean $\overline{[\mu/\rho]}$ at that energy. The absolute uncertainty is then

$$\frac{(\Delta_{[\mu/\rho]})_a}{[\mu/\rho]} = \sqrt{\left(\frac{(\Delta_{[\mu/\rho]})_r}{[\mu/\rho]}\right)^2 + \left(\frac{(\Delta_{[\mu/\rho]})_{ff}}{[\mu/\rho]_{ff}}\right)^2}, \tag{7}$$

were the *ff* subscript represents the full foil mapping result uncertainty. The two types of uncertainties play important roles in different analyses: the relative precision is the correct uncertainty when comparing to relative XAFS predictions of e.g. IFEFFIT, whereas the absolute uncertainty is relevant when comparing to theory of *ab initio* XAFS calculations such as FDMX or FEFF.

4. Sources of systematic error

Our previous experiments employing the XERT have been of high enough accuracy to detect and allow correction for multiple systematic errors when making absorption measurements. This is crucial in demonstrating the reproducibility of results and permitting absolute tests of theory.

This includes but is not limited to: energy calibration [23, 24] and correction of lattice parameters [25, 26], scattering and fluorescent radiation [27, 28], detector non-linearity [29] and harmonic contamination [30, 31], nanoroughness [32] and finite spectral-bandwidth [33]. We show that harmonic contamination and fluorescent radiation in this work were not significant factors, whilst the bandwidth of the beam had a large impact upon foils of different thickness near the absorption edge.

4.1. Bandwidth

Ideally, the Si (311) monochromator allows reflections from x-rays of energy corresponding to the fundamental reflection plane of the crystal. However complex broadening effects mean that the energy of the beam is a spectrum of energies, described by an intensity profile with respect to energy. Photons whose energy differs from the fundamental energy due to broadening processes cause systematic shifts in the measured mass attenuation coefficient. Following the prescription of de Jonge *et al* [33], the Beer–Lambert law is recast as

$$\exp\left\{-\left[\frac{\mu}{\rho}\right][\rho t]\right\} = \frac{\int_0^\infty I_d \mathrm{d}E}{\int_0^\infty I_u \mathrm{d}E}, \tag{8}$$

where I_u and I_d represent the energy-dependent intensity profiles recorded by the upstream and downstream detectors respectively. If I_u is assumed to be a normalised Gaussian profile with respect to energy, with a standard deviation of σ then the correction due to bandwidth becomes

$$C_{E_0} = \left[\frac{\mu}{\rho}\right]_{t,E_0} - \left[\frac{\mu}{\rho}\right]_{m,E_0} \tag{9}$$

$$= \frac{\sigma^2}{2}\left[\left[\frac{\mu}{\rho}\right]'^2_{tE_0}[\rho t] - \left[\frac{\mu}{\rho}\right]''_{tE_0}\right], \tag{10}$$

where $[\mu/\rho]'_{tE_0}$ is the first order derivative of the mass attenuation coefficient with respect to energy, and similarly $[\mu/\rho]''_{tE_0}$ is the second order derivative. This shows that the correction factor due to bandwidth depends on the thickness of the sample and the first and second order derivatives of the mass attenuation coefficient with respect to energy. The bandwidth therefore presents a clear signature in the weighted mean of the mass attenuation coefficients for different sample thicknesses, as shown in figure 4.

A correction due to bandwidth was added to the fitting procedure, where the width of the Gaussian was fitted as a free parameter. Without including corrections due to bandwidth, the goodness of fit was $\chi_r^2 = 3.6$ compared with adding the correction due to bandwidth which yielded a goodness of fit of $\chi_r^2 = 2.0$. This reduction in χ_r^2 shows that bandwidth had a significant affect on measurements and was able to be successfully determined from the measurements with multiple foils. The correction was applied over the whole energy range and was determined to correspond to a FWHM $\sigma = (8.79 \pm 0.18)$ eV.

Our new analytic form of the correction due to bandwidth was tested with respect to previously used numerical methods. The two methods were in agreement to within their respective error bars. The new analytic form was used in the final results and is faster and a more accurate prescription of the first order effect. The determination and accuracy of this result is a key step towards the cross-platform portability of data, and in particular the possibility of determining a unique theoretical and experimental value of the Fermi energy or the 'energy offset' E_0. We observe and correct for the effect of bandwidth on the absorption edge, causing significant discrepancies between foils of different thickness, and between different experiments with the same sample at different beam lines with different divergence or bandwidth.

4.2. Harmonic contamination

The Si (311) double reflection monochromator naturally suppresses second order harmonics as this is a forbidden reflection due to the symmetry of the crystal. The third order reflection is allowed, but is also suppressed due to depth penetration. Linearity across all foils was investigated by inspection of the attenuation versus integrated column density plots. No deviation from linearity was observed, suggesting no measurable harmonic contamination (as opposed to other high-accuracy experiments [33, 34]).

4.3. Secondary photons

Secondary photons are of particular concern as they cause unwanted events in the ion chambers, leading to inaccurate count rates. Most significant are fluorescent photons produced by incident energies above the absorption edge. The most common process is that of L-shell electrons decaying to the unoccupied K-shell due to the ionisation of the 1s electron. The dominant line is the $K\alpha_1$ line producing a fluorescent photon of approximate energy 22.163 kev. Unwanted fluorescent photons are suppressed due to multiple small apertures located on each of the daisy wheels. The three different solid angles provided by each aperture permits rigorous analysis of aperture dependence on the measured mass attenuation coefficients. As the ion chambers are located far from the sample in a symmetric geometry, it is expected that any fluorescent photons will have an undetectable and insignificant effect on the measured mass attenuation coefficients.

A general approach was adopted to investigate the effect of all secondary photons. In this manner, we inspect the significance of deviations between each of the apertures

$$\text{significance} = \frac{\left[\frac{\mu}{\rho}\right]_{\text{larger}} - \left[\frac{\mu}{\rho}\right]_{\text{smaller}}}{\sqrt{\sigma^2_{\text{larger}} + \sigma^2_{\text{smaller}}}} \tag{11}$$

where the larger and smaller subscripts refer to larger and smaller sized apertures respectively, and σ is the associated uncertainty with the measurement. There was no apparent structure in the significance in relation to the different sized aperture, and no significant deviation from the zero line. Most deviations were well within 1σ of the experimental uncertainties, and none exceeded 2σ, demonstrating no significant effect from secondary photons [27].

5. Determining the photon energies

The photon energies were determined by recording powder diffraction patterns of NIST SRMs LaB_6 (660a) and Si (640c) using the high resolution powder diffractometer BigDiff [35, 36]. Powder diffraction has advantages in that many diffraction peaks can be recorded simultaneously permitting rigorous tests of experimental errors.

Powder patterns were recorded at regular intervals during the experiment generally covering a diffracting region of $-45° < 2\theta < 45°$ and up to $-135° < 2\theta < 45°$ at lower energies. Each diffraction peak profile was fitted with a Gaussian convolved with a slit, on a constant background in order to determine accurate values of the peak positions. Our group has previously used Lorentzian profiles to fit powder diffraction peaks, however in this case Gaussian peaks were better suited to the data and generally had a χ_r^2 value half that of the Lorentzian peaks.

Weak peaks of insufficient height and peaks whose slit width was large were excluded from the fitting procedure. At the highest energies (28 keV) there were some 60 peaks fitted. The number of peaks became more sparse as expected towards lower energies, with about 21 peaks at 13 keV and 8 peaks at 8 keV, still suitable for a high-accuracy determination. Each peak was then assigned a *hkl* Miller index in a highly automated procedure. It is important that all non Bragg reflections are removed before this procedure, as spurious peaks cause confusion in the assignment of the *hkl* values.

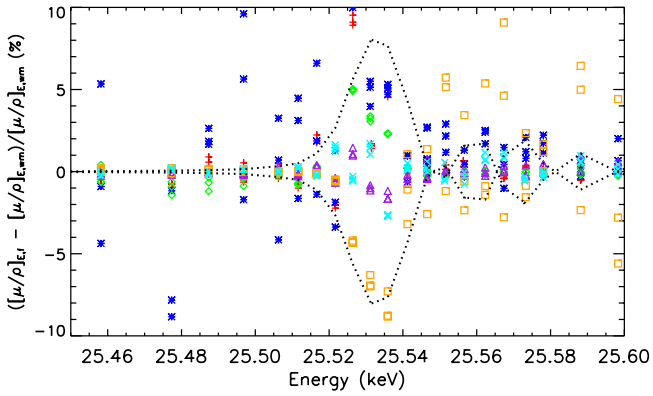

Figure 4. Percentage deviation from the weighted mean in the vicinity of the absorption edge shows a clear systematic directly on the absorption edge. The dotted line represents the relative form of the gradient of the mass attenuation coefficient with respect to energy.

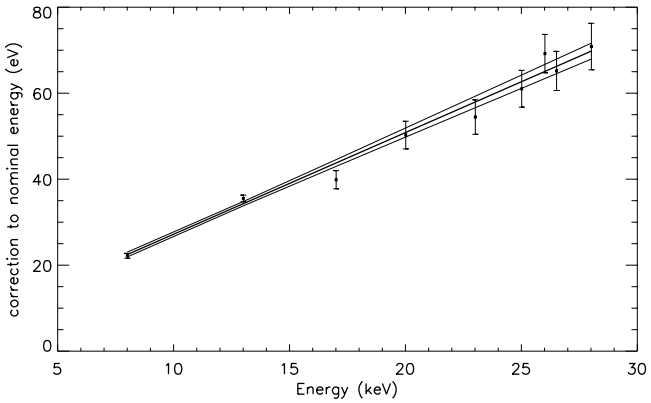

Figure 5. Calibration curve of the photon energies. Correction to the nominal energy of the monochromator using powder diffraction. Offsets of up to 70 eV are seen highlighting the importance of accurate energy calibration.

Once each peak had been assigned the correct *hkl* value, each peak in the powder pattern was simultaneously fitted to our modified form of the Bragg equation

$$\sin(\theta + \delta\theta_{P_i} + \delta\theta_y + \delta\theta_z) = \frac{hc}{2dE_{\text{cal}}}, \tag{12}$$

with

$$\delta\theta_y = \frac{\delta_y}{R}\cos 2\theta, \text{ and} \qquad \delta\theta_z = \frac{\delta_z}{R}\sin 2\theta, \tag{13}$$

where δ_y and δ_z are the small vertical and horizontal sample offsets in alignment of the beam from the centre of BigDiff, R is the radius or the distance from the capillary to the image plates, θ_{P_i} is the image plate offset for the ith plate, d is the distance between adjacent diffraction planes and the other parameters have their usual meanings.

The peaks were firstly fitted with each separate plate in a separate fitting procedure. This worked well at lower energies, however at higher energies the horizontal powder offset became highly correlated with the determined energy and hence had large uncertainties. The fitting procedure was then altered so that patterns with common image plate offset and energies were fitted simultaneously in order to constrain the horizontal offset and image plate offsets. This improved results slightly, however the horizontal offset was still highly correlated with energy at high energies.

A final iteration fitted all peaks simultaneously, constraining the horizontal offset to a constant value for all of the data. The goodness of fit, measured by $\sqrt{\chi_r^2}$ was 3.7 suggesting the model was accurate.

The results of the energy calibration are presented in figure 5 and tabulated in the appendix (table A2). A straight line was fitted to the difference between the calibrated and nominal energies. The linear trend is clear, and shows offsets of up to 70 ev at the highest energies.

6. Results and comparison with previous work

We have so far focused on measurements of the total mass attenuation coefficient of silver, for which a summary of the typical uncertainties and error budget is presented in table 1. This includes all scattering processes involved in the removal of photons from the x-ray beam. The imaginary component of the form factor f_2 requires removal of elastic and inelastic scattering coefficients to determine photoelectric mass attenuation coefficient. The total attenuation in the relevant x-ray energy regime can be approximated as a sum of the major contributing scattering processes:

$$\left[\frac{\mu}{\rho}\right]_{\text{tot}} \approx \left[\frac{\mu}{\rho}\right]_{\text{pe}} + \left[\frac{\mu}{\rho}\right]_{\text{R}} + \left[\frac{\mu}{\rho}\right]_{\text{C}}, \tag{14}$$

where the attenuation components respectively are the total, photoelectric, Rayleigh (elastic) and Compton (inelastic) scattering. Subtraction of the Rayleigh and Compton components from the total measured attenuation yields the photoelectric absorption coefficient, which is used to calculate the imaginary component of the atomic form factor f_2

$$f_2 = \frac{EuA[\mu/\rho]_{\text{pe}}}{2hcr_e}, \tag{15}$$

where, E is the x-ray energy in eV, u the atomic mass unit, A is the relative atomic mass (of silver), h is Planck's constant, c the speed of light and r_e is the classical electron radius. There is an additional uncertainty included in the determination of $[\mu/\rho]_{\text{pe}}$ which comes from half the difference between the two tabulations used to determine the Rayleigh and Compton components of the total absorption cross section. These values are given explicitly in table A2 in the appendix A.

This work represents the first XERT measurement of silver over an energy range inclusive of the K-edge XAFS spectrum, with sufficiently high density of data collection to elucidate the detailed oscillatory structure and hence solid-state properties of the system. We compare our experimental results to previous measurements and tabulations of the mass attenuation coefficient of silver which possess overlap in parts of our studied energy range. The measurements presented in figure 6 of Tran *et al* [19] span the energy range 15–50 keV, while measurements from Islam *et al* [34] span the energy range 5–20 keV. Various measurements from Sandiago [37] and Tajuddin [38] are also included. Figure 6, in addition to theoretical data from the FFAST [40–42] and XCOM [42] tabulations.

Table 1. Error contributions to the values reported in table A2, with source specified.

Quantity	Estimated magnitude	Contributions & comments
		Away from the absorption edge
$\left[\frac{\mu}{\rho}\right]$	0.03%	accuracy limited by the full-foil mapping technique (appendix A.1)
	0.01%–0.07%	precision, limited by counting statistics and variation between foils
		Near the absorption edge (25.5 kev–26 kev)
$\left[\frac{\mu}{\rho}\right]$	(0.0 → 0.3)%	x-ray bandwidth (section 4.1)
	<0.01%	harmonic components (section 4.2)
	<0.01%	secondary photons (section 4.3)
E	0.005%–0.017%	accuracy of monochromator dispersion function interpolation (section 5)
f_2	0.1%–1%	inconsistency of subtracted scattering components (section 6)

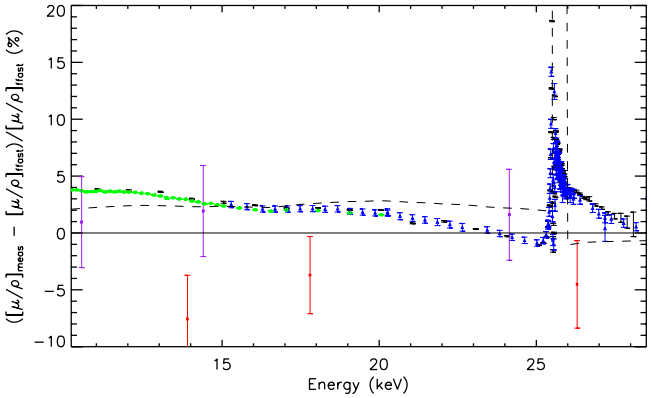

Figure 6. Comparison with FFAST [40–42] as the zero line, this work—black error bars, Tran *et al* [19]—blue diamonds, Islam *et al* [34]—green boxes, Sandiago *et al* [37]—purple stars, Tajuddin [38]—red crosses and the XCOM database [42] as the dashed line.

Figure 6 shows clear deviations from both FFAST and XCOM, which varies across different energy regions. Above the K-edge, a systematic triangular-shaped discrepancy is clear in both this work as well as the work of Tran [19]. Attenuation levels above edges have been consistently observed to be higher than theoretical computations. Some modelling has explicitly included an attenuation enhancement in this region when fitting mass attenuation coefficients to theoretical tabulated values [43], and it is typical for XAFS analysis packages to use some sort of spline function to overcome the discrepancy. Creagh has observed that the possible enhancement could be attributed to some new scattering mechanism [45–47]. Our group has observed a consistent pattern in several materials, which we call here and elsewhere *the triangle effect* [22, 47].

The consistency of this work with previous studies highlights the reproducibility of the XERT to within the quoted uncertainty, independent of the experimental beam line. Variations exist up to around 20% around the K edge, particularly for XCOM. At the higher energies presented here, there seems good agreement to 1% or better. At lowest energies measured, discrepancies reach 2%–4%, depending upon model. However, the XERT experimental works remain consistent at all energies to within their small claimed uncertainties of order 0.1%.

7. Comparison with solid state theory

X-ray Absorption Spectroscopy and XAFS investigate the oscillations of the photoabsorption coefficient above the threshold due to the photoelectron interference. Conventionally the XANES (near-edge) region is assessed relative to markers or standards—such as silver—which is not helpful for the calibration of a standard. Further, fitting of the Extended X-ray Absorption Fine Structure (EXAFS) is usually truncated at values of effective photoelectron momentum 3 $\text{Å}^{-1} < k <$ 15 Å^{-1} or so, has an empirical spline function removed, is scaled with unknown uncertainties, and fitted. While it has been proven of great value in confirming active centres, dynamic structures and local ionisation states, it is not a particularly *ab initio* method and discards any information from the XANES region of the spectrum.

Our approach is to attempt to fit the whole XANES and EXAFS region with a single theoretical and computational approach in a manner which can then solve structures in an *ab initio* sense, allowing critical appraisal of the significance and value of any structural model. To illustrate this process we present an advanced development of one of the standard approaches for XAFS analysis, that of FEFF and IFEFFIT [48, 49]; and then contrast this with a new computational package FDMX [11, 50], developed by this group, following Joly and his FDMNES approach [8, 51].

8. FEFF8 analysis

The experimental data was fitted to FEFF8 theoretical output [52] through the IFEFFIT program. We use a modified IFEFFIT structure to preserve the uncertainties and statistical significance of the information content from individual data points [49]. The scattering paths output by FEFF are used by IFEFFIT to fit the experimental results to theory and permit the extraction of information regarding the local structure of silver. In this case 26 independent scattering paths, of varying degeneracies, were considered in the calculation. The oscillatory part of the measured spectrum, $\chi(k)$ was then isolated via a standard spline function in order to compare with theory.

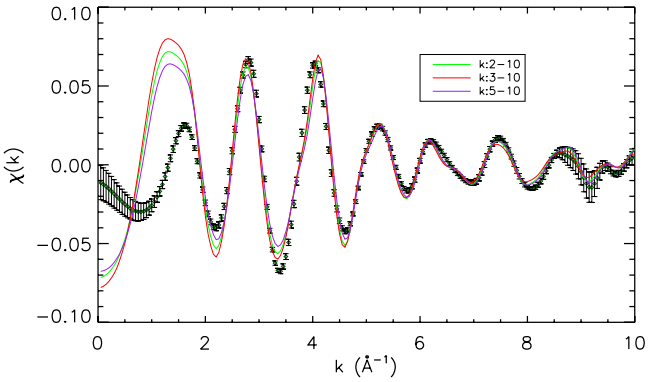

Figure 7. IFEFFIT plots refined over different k windows, with uncertainties propagated. Structures are robust and appear well-fitted, though the restricted k-range leads to a comfortable χ_r^2 for the reduced region of interest.

The results for optimised fitting using different k windows are shown in figure 7.

Table 2 lists our derived parameters from the IFEFFIT analysis based on each fitting window, and is in accord with the conventional understanding that including a large k-range in the fitting and especially to low k-values such as $k = 2$ Å^{-1} gives relatively high χ_r^2. The figure also shows clearly that large deviations occur outside the Hanning windowed region.

Unlike such discussion in past literature, however, in this analysis the χ_r^2 values are well-defined across the relevant ranges and rigorously determined by the experimental uncertainties. While one can argue that a $\chi_r^2 \gg 1$ implies a model error, an underestimate of the input experimental data point uncertainties, correlated systematics or indeed an unphysical model, we simply note here that the information content is sufficiently strong to confirm the significance of the improvement of χ_r^2 with an improved, more complete and more physical model and that the final result here is encouraging.

With respect to our key parameters of current interest, it demonstrates that the imputed Debye–Waller parameter (σ^2 or $\bar{u}^2$) appears stable at around $\sigma_{\mathrm{DW}} = 0.1$ Å or perhaps 0.095–0.11 Å (i.e. ±17%). We note that the fitting uncertainty for each range is approximately 10% but that the model dependence dominates so that a fairer estimate is $\sigma\sqrt{\chi_r^2}$ or 30%–40%. Even within this uncertainty, however, the value from IFEFFIT is significantly reduced from several literature values, which have been aggregated by Butt *et al* to be 0.173(2) Å [54]. The sources of this data are primarily x-ray powder diffraction experiments [56–60], corrected via a theoretical model of thermal diffuse scattering [60]. The source of this discrepancy may be elucidated from our analysis using the new FDMX package in the following section.

The scaling of the lattice parameter (or bond length) from that of the nominal value of 4.0853 Å [53] is somewhat unclear from the IFEFFIT results. Certainly one may take the higher-energy fitting window as the most plausible guide given its relatively low value of χ_r^2, however given the variation in α values from 0.0024 to −0.0023 (and large uncertainties), this result is to be taken with some skepticism. Part of the difficulty in this analysis is that, as demonstrated by figure 7, IFEFFIT cannot accurately model the near edge structure in the full XAFS spectrum due to limitations of its theoretical implementation. This also imputes that the fit over 2 Å$^{-1} < k <$ 10 Å^{-1} should be considered as outside the normal range of validity.

Table 2. Fitted parameters for different IFEFFIT-like fits.

k-range	σ_{DW} (Å)	α	χ_r^2
–10	0.101 (41)	0.0003 (160)	13.8
–10	0.112 (43)	0.0024 (210)	12.8
–10	0.095 (15)	−0.0022 (62)	2.2

IFEFFIT does not conventionally report spline fits and accuracy, but does provide fitting of S_0^2 and E_0 in particular, together with (an effective) Debye–Waller thermal parameter σ_{DW} and a scaling of the input lattice parameter or bond length by $1 + \alpha$. Our values for α are based on a nominal lattice parameter of 4.0853 Å [53].

Nonetheless, the results from figure 7 do show excellent agreement with the experimental data in the high-energy region above $k = 5$ Å^{-1}. Indeed in this range the agreement of theory and experiment is remarkable, with a χ_r^2 value of 2.2 being particularly striking given the strong absolute accuracy of the measurements (often below 0.1% in this region). The theory also manages to remain qualitatively accurate down to wave number values of $k = 2$ Å^{-1}.

This is partly achieved by the rigour of the computational technique at high energies, and partly by the use of a detailed empirical spline function to remove the triangle effect discrepancy at low energies. This spline function is, however, a concerning feature as it includes oscillatory structure that may be used to artificially improve the goodness of fit despite possible shortcomings in the XANES calculation. Further, the theory is poorly suited to low-energy analysis due to approximations in the electrostatic potential currently necessary for multiple-scattering calculations.

9. FDMX

We have developed a new package FDMX which permit simultaneous analysis of the full edge region, the XANES and the EXAFS region. This is a development of the Finite Difference Method for Near-Edge Structure (FDMNES) package [8]. This package solves the Schrödinger equation on a discretized grid to avoid assumptions made about the potential such as the muffin-tin approximation. Key inputs into the program for efficient and robust convergence are the cluster size radius, which determines how many atoms are present in the calculation, and the grid spacing, the distance between neighbouring spatial computational points. At increasing energies the cluster size may be reduced due to the waning significance of far-reaching scattering paths, however the grid density must be increased significantly in order to properly represent the high-frequency wave function. Parameters used for this calculation are given in table 3, and were checked for convergence by overlapping of the energy regions.

Table 3. Computational parameters for the FDMX calculation of silver XAFS over various energy ranges.

Range (eV)	R (Å)	h (Å)
−10 to 50	8.0	0.20
50 to 150	6.0	0.15
150 to 300	5.0	0.1
300 to 400	4.0	0.1
400 +	3.5	0.1

R is the radius of the cluster and h the interpoint distance, determining the grid density.

The FDMX program incorporates major advances in processing power and efficiency, understanding of broadening in x-ray absorption, thermal broadening [9], and inelastic scattering [11, 12], leading to results significantly in advance of our previous silver cluster calculations [61]. The use of FDMX, by contrast with other full-potential modelling, enables robust *ab initio* computation of x-ray absorption coefficients from below an absorption edge, through the XANES and XAFS regions, and right up to keV energies where atom-like spectra are observed [50, 62].

Core-hole and photoelectron lifetime broadening are implemented via convolution of raw (lossless) spectra with Lorentzian profiles. The core-hole width is assigned following the tabulations of Krause and Oliver [63], while the photoelectron lifetime is determined from the electron inelastic mean free path (IMFP) for an electron of energy $E - E_0$. The IMFP is calculated via a self-consistent algorithm based on optical data modelling [64], which is coupled with optical oscillator strengths calculated using density functional theory [65, 66]. The hole width is constant for all energies, while broadening due to inelastic scattering is dynamic and changes with photoelectron energy. The total broadening is then given by

$$\Gamma(E)_{\text{total}} = \Gamma_{\text{hole}} + \Gamma(E)_{\text{inelastic}}, \tag{16}$$

where, for silver, the value of Γ_{hole} is taken to be 6.42 eV.

9.1. The fitting procedure

The fitting procedure within FDMX requires a unique parameterisation of the absorption spectrum in order to isolate the key oscillatory structure without the use of empirical spline functions. This enables quantification of individual structural parameters based on a fit of the oscillatory structure to the experimental spectrum, and has been used previously to determine highly accurate inelastic scattering data [11, 12]. This is the first time such an approach has been utilised to extract lattice spacings and thermal parameters. The mass absorption coefficient from FDMX is represented as follows:

$$\left[\frac{\mu}{\rho}\right]_{\text{FDMX}}(E) = \left[\frac{\mu}{\rho}\right]_0(E) \times [(1+T)(1+\chi)] + \left[\frac{\mu}{\rho}\right]_{\text{BKG}}(E), \tag{17}$$

where $\left[\frac{\mu}{\rho}\right]_0$ is the atomic background function, $T = P_1 \times \exp\{-P_2 \times E\}$ is an exponential function of energy giving an approximation to the triangle effect, χ is the oscillatory part of the spectrum (which is thermally broadened) and $\left[\frac{\mu}{\rho}\right]_{\text{BKG}}$ is the non k-shell photoelectric absorption contribution to the spectrum, which may be taken from the FFAST database [40], which has demonstrated accuracy well away from absorption edges.

9.2. Edge energy

As with conventional XAFS analysis, the theoretical spectra were shifted along the energy axis in the fitting procedure to match the experiment. Key systematics in both experimental data collection and in theoretical modelling usually enforce this requirement. In our case the experiment has an absolute energy to an accuracy of 1.6 eV; however, this does not impute a clear determination of the ideal edge position to that accuracy, nor does it address or fix all systematic uncertainties in the theoretical computation and convergence.

The combination of our absolute energy calibration during experiments and free parameter in the fitting procedure permit high accuracy determination of the K-edge energy for applications including chemical shifts, pre-edge evaluation and XANES feature analysis. This parameter transforms the energy such that $E \to E - E_{\text{edge}}$. This offset was very stable over the various fits performed to determine the Debye–Waller factor and lattice parameter, suggesting minimal correlation between these parameters.

Adding the energy offset to the FDMX output shifted the edge energy from the nominal FDMNES output of 25.514 keV to 25.5183(25) keV, or a shift (of theory) of (4.3 ± 2.5) eV—not much larger than the explicit energy calibration uncertainty. Adding the edge energy as a free parameter is required to reduce discrepancies between theory and experiment and allows robust quantitative fitting of key physical properties. We note, perhaps surprisingly to some, that accounting for the edge energy shift decreased χ_r^2 'only' from 26 381 to 25 796! Be clear that the model failures at this point in the fit and convergence are enormous—however with subsequent refinements we are able to investigate causes and solutions of these model limitations.

9.3. Triangle function

After adding the energy offset, there remains very large discrepancies between theory and experiment. This discrepancy is also present in figure 6 when compared to atomic absorption theory—see the earlier discussion of the evidence for this commonly observed discrepancy. Causes of the discrepancy are likely theoretical, and the exponential chosen here clearly has limitations to be addressed in the future. The form of the discrepancy in both cases is approximately trapezoidal in the energy and absorption axes. The fit was originally performed with a trapezoid, but an exponential function is a much better approximation. The function then used had the form $T = P_1 \times \exp\{-P_2 \times E\}$, where the parameter P_1 scaled the function in the absorption axis and the parameter P_2 stretches the function over the energy axis. Adding the exponential

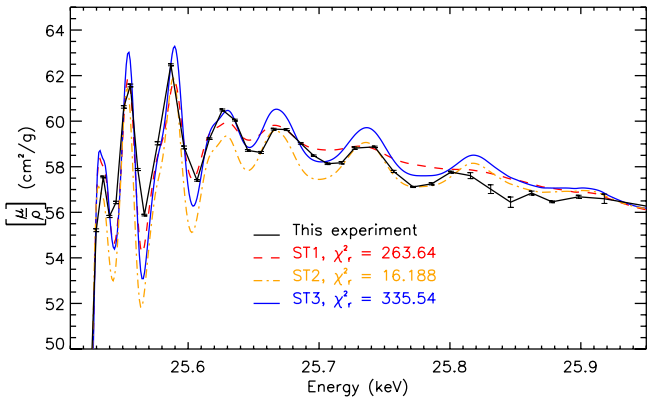

Figure 8. Comparison of experiment with solid theory. ST1 has a free DW factor and includes all peaks, ST2 has a free DW but only includes peaks above 25.72 keV (note that the fit is quite good over this range) and ST3 includes all peaks and has a fixed DW which is taken from ST2.

function (including the edge energy offset) reduced χ_r^2 from 26 381 to 14 112, nearly halving χ_r^2.

While this is a clear advantage, numerous standard packages use an empirical spline fit to remove this background. The spline also removes or adds a low-order, relatively-smooth functional dependence of the discrepancy of absorption from theory above the edge. The spline proscription therefore may be used for long energy-range analysis of parameters, but potentially corrupts the oscillatory XAFS signal due to this dependence, and therefore we avoid such an approach in this work.

9.4. Debye–Waller factor

The XAFS spectrum is broadened by inelastic scattering and hole widths calculated within the FDMX package, together with thermal signal reduction by $e^{-2\sigma_{DW}^2 k^2}$, where σ_{DW} is the Debye–Waller factor and k is the effective photoelectron wave number.

The black line and black error bars in figure 8 are the experimental photo-absorption results presented in this work. The red line is the result of an FDMX computation, where the Debye–Waller factor is fitted for the entire energy range of the spectrum, which we will call solid theory 1 (ST1). This calculation worked well for intermediate energies, producing a fitted DW factor of $\sigma_{DW} = 0.169(11)$ Å, but did not adequately describe the magnitude of the oscillations at higher photoelectron energies (the signal was overdampened). Nonetheless, the reader may be surprised that the χ_r^2 is now only 264. A high and unacceptable value to be sure, but much improved over the fit only involving the edge offset and the exponential. The major change is from excluding the below-edge and edge-jump discrepancies, and focussing on the above-edge structure. It should be realised that these parameters are commonly strongly correlated, so it is often important to determine one parameter on relevant evidence for that parameter and then constrain it and work with subsequent parameters. This approach is generally well-known for any complex multi-dimensional correlated space.

Table 4. Results of various fitting procedures.

Parameter	ST3	ST1
Energy offset	25 521.73 (32) (eV)	25 521.61 (33) (eV)
σ_{DW}, Debye–Waller	0.1281 (fixed) (Å)	0.169 (11) (Å)
P_1 (triangle)	0.1621 (57)	0.1633 (52)
P_2 (triangle)	0.001 68 (18) (keV^{-1})	0.001 77 (17) (keV^{-1})
χ_r^2	335	236

ST1 has a larger DW factor as it is dominated by early XAFS peaks. ST3 uses the DW factor determined in ST2 which used only higher photoelectron energies.

Therefore, the yellow-orange line in figure 8, which we call solid theory 2 (ST2), fitted energies only above 25.72 keV and resulted in $\sigma_{DW} = 0.1281(31)$ Å. This fit allows the DW factor to be fitted only for higher photoelectron energies, where the DW factor is of greatest effect. For this subset of data, we find $\chi_r^2 = 16$—much lower than for ST1 due to the smaller region used in the fit, showing as with the FEFF analysis that the theory tends to be more consistent over appropriately windowed energy ranges. This energy dependence is troublesome, however, and raises some key issues:

Does the effective σ_{DW}^2 change across the energy range in XAFS? The evidence suggests that this may be true.

Can our modelling, like that of more conventional approaches, only operate at one range of k-space? Our model seems to function well across limited but variable ranges. This limitation is primarily due to the residual discrepancies due to the triangle effect and the exponential function fitted to remove or account for it. However, it is also affected by any variation of the constancy of the fitting parameters across the k-range.

While the user may keenly wish to just get a publishable value for bonding or structure or thermal parameters, we feel that presenting the magnitude and impact of different approximations is critical. And the correlation between them imputes a risk from neglecting their contributions.

In ST3, the value of the DW factor from ST2 was used as a constraint in the fit over the full above-edge energy range. Parameters associated with the ST1 and ST3 fits are provided in table 4. While the χ_r^2 has necessarily increased, it shows the impact of a different optimisation and the fact that the lower-k-range requires additional broadening in that region. This suggests that using a single parameter for the the DW factor is inadequate for describing XAFS oscillations over extended energy ranges. This is not surprising as the photoelectron interacts with neighbouring atoms of varying distance at different energies and suggests that the DW factor for XAFS should be represented by more than one parameter depending on the chosen energy window.

9.5. Silver bond length

In the case of this data set, the scale factor $1 + \alpha$ in the XAFS equation dictates not only the possible lattice spacing and solid state periodicity but also the silver metal bond length, which differs from the lattice spacing by a factor of $1/\sqrt{2}$.

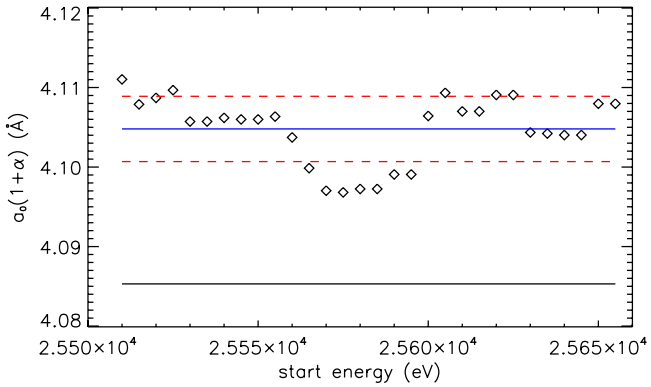

Figure 9. Comparison of imputed bond-length as a function across fitting ranges above the edge. Excellent consistency is attained, demonstrating the stability and reliability of this parameter to approximately 0.1% accuracy: $\alpha = +0.5\% \pm 0.1\%$; $a_0(1+\alpha) = 4.106 \pm 0.004$ Å.

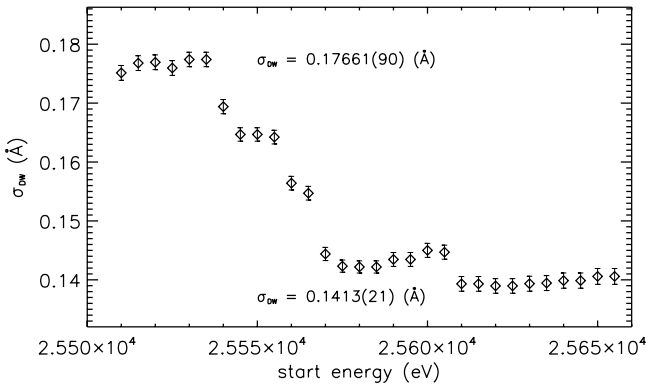

Figure 10. Comparison on imputed Debye–Waller factors across different fitting ranges of the XAFS spectrum. Two stable values appear: one at lower energy and one at higher energy ranges. Individual error bars plotted are fitted σ values given the input data uncertainties.

While the results of figure 8 appear to show good alignment of the periodicity, and hence a good first estimate, there are deviations from this fit which contributes significantly to χ_r^2.

The bond length between neighbouring atoms was therefore fitted within the FDMX computation from a default value of $a_0 = 4.0853$ Å as given by Liu and Bassett [53]. Several alternate literature sources are available for the lattice parameter/bond length of elemental silver, with most measurements being made using x-ray powder diffraction with values reasonably ranging from $a_0 = 4.071$ Å [67] to $a_0 = 4.0862$ Å [68]. More recent work using XAFS fitting similar to our IFEFFIT analysis determined the lattice parameter of silver to be 4.093 Å [69].

To orthogonalise the lattice parameter uncertainty, four values (E_0, σ_{DW}, P_1, P_2) were fitted for the original value of a_0, and then applied to the convergence of the lattice parameter with the only additional free parameter being σ_{DW}. In this way, correlations between the lattice parameter, the energy offset, and triangle parameters are suppressed.

This was done over an extended parameter space with varying energy windows used in the fit. The initial energy window started at 25.510 keV and extended for 200 eV in the XAFS spectrum. The region was then shifted +5 eV, 30 times, to investigate parameter evolution for different energy fitting windows. The set of local minima in χ_r^2 between the different bond-length parameters over a range of fitting regions, corresponding to the best-fit lattice parameters for each subset of data, is shown in figure 9.

From figure 9 we find that the best fit for the lattice parameter is $+0.5 \pm 0.1\%$ higher than the given value of $a_0 = 4.0853$, giving $a_{new} = 4.1057(41)$. This is slightly higher than the value given by Dubiel *et al* from their XAFS analysis [69]. The best-fit lattice parameter is somewhat dependent on the energy range of the fit, but we find that overall there is a good consistency around our final value.

Given this value of the lattice parameter from our fitted data, we are able to make a more detailed investigation of the Debye–Waller factor as a function of energy. Figure 10 shows a similar analysis of the best-fit Debye–Waller factor using 200 eV energy ranges with different starting points covering much of the XAFS spectrum.

This result shows a much stronger energy dependence than for the lattice parameter, and illustrates a clear physical phenomenon whereby the effective Debye–Waller factor transitions from a low-energy value to a high-energy value. The values of χ_r^2 vary somewhat across the spectrum, from around 16 for low-energy windows down to as low as 8 for high energy windows, meaning that with a full set of included parameters the FDMX technique can produce absolute XAFS results comparable with those of FEFF/IFEFFIT. Although the match is still not ideal, prominently due to weaknesses in the triangle function, the stability of the curve in figure 10 suggests that the existence of two separate Debye–Waller parameters in the XAFS spectrum is real.

Such a model is not necessary for crystallographic measurements, but is quite justified in XAFS by the underlying physics. The oscillatory XAFS structure arises due to backscattering contributions from neighbouring atoms with varying distance from the photo-absorbing atom. These contributions possess different oscillatory frequencies based on the atom–atom distances, with nearby atoms contributing lower frequencies, and also possessing a relatively lower thermal contribution due to their strongly correlated motion with the absorber. This correlation commonly leads to a differentiation between the (uncorrelated) DW factor given by crystallography, and the DW factor normally extracted from XAFS [70]. At higher energies in the XAFS spectrum, inelastic scattering effects become dominant, filtering out high-frequency contributions from far-away atoms in the material, leaving the low-frequency contributions to become dominant, hence revealing a low DW factor corresponding to the first co-ordination shell.

At low XAFS energies where inelastic scattering is relatively minor, contributions from uncorrelated, far-away atoms, and also uncorrelated contributions from multiple scattering (MS) paths become significant [71]. Although the cross sections for these paths are lower than for the shorter single scattering paths, they have a much higher degeneracy and

result in fine oscillatory structure near the absorption edge. The thermal damping of these oscillations therefore becomes dominant in the fit for the DW factor, and yields a higher value corresponding to the bulk DW factor normally measured in crystallography.

The dependence of σ_{DW} on the co-ordination shell and scattering path-length in XAFS is a topic that was raised in early work by Stern *et al* [72], and is also the subject of more modern investigations via cumulant paramaterisation in Fourier Transform analyses [73]. This work is the first to identify two distinct regions of dominance in the thermal parameter, and we attribute this outcome to the characteristic shape of the broadening contribution from inelastic electron scattering, which undergoes a clear transition at intermediate XAFS energies [11]. In fact, the broadening function derived from the IMFP of silver predicts that the critical point for transition between low-energy and high-energy behaviour is approximately 250 eV, which falls roughly in the middle of the range measured in figure 10 when the starting energy is 2.557 keV.

The high-energy DW factor (for the first co-ordination shell) is measured to be $\sigma_{DW} \approx 0.1413(21)$ Å, which is slightly higher than that derived from the IFEFFIT analysis. We believe this is primarily due to differences in the implementation of the triangle effect, which become significant over large energy ranges. In particular, the spline functions used in IFEFFIT commonly subtract some low-frequency components from the XAFS spectrum, which may artificially reduce the measured DW factor. Our measured low-energy DW factor (for the bulk material) is $\sigma_{DW} = 0.1766(9)$ Å. This is in remarkably good agreement with the value given by crystallography, $\sigma_{DW} = 0.173(2)$ Å [54].

10. Conclusion

Carefully designed experiments aimed at identifying all possible systematic sources of error with high precision absorption measurements over a wide parameter space can produce extremely high accuracy absolute measurements of the mass attenuation coefficient and the imaginary component of the x-ray form factor f_2. In figure 6 we have demonstrated the robustness and beam line independence of the experimental approach, with excellent agreement observed with previous work by Tran *et al* [19] and Islam *et al* [34]. This agreement is within 1σ over all measured energies and, given the high accuracy overall of within 0.1%, this enables critical interrogation of physical parameters that possess XAFS signatures over a broad energy range.

Though the methodologies presented require a higher level of investment and sophistication than standard approaches, they can be readily repurposed for measurements of inorganic systems, organometallics and even dilute solutions. The beam-time requirements of the XERT depend upon the detailed set-up and available flux and instrumentation; but in general the overhead to achieve 100 times the accuracy and precision is usually less than a factor of three in beam-time. This trade-off is particularly good value given that interrogation of complex chemical systems at such high accuracies will prove invaluable for examination of subtle variations in XAFS spectra, allowing significant advances in co-ordination and conformational chemistry [74].

Our XAFS calculations from both FEFF and FDMX show strong agreement with experiment over critical energy ranges, with χ_r^2 values of 8 or less even for our most highly accurate measurements. Our developments of IFEFFIT for the rigorous propagation of uncertainties allows a more robust evaluation of physical parameters, while our development of FDMX allows a new methodology with robust applicability over the entire energy range of XAFS.

The results from FDMX represent the first rigorous parameterization of lattice spacing and thermal parameters from XAFS using a full-potential computational model. Previous studies have been limited to approximate-potential models, such as our FEFF analysis, or XANES modelling in the absence of robust high-energy theory [75]. The ability to fit full-potential theory across the entire XAFS range with similar accuracy to the more established multiple scattering theory is therefore a significant achievement which will see widespread application to a number of more complex chemical systems for which full-potential modelling has been shown to be necessary in the low-energy XANES regime [76].

The significance of the result is further enhanced by the energy-dependence of the extracted parameters. Unlike the results from modified IFEFFIT, the lattice spacing from FDMX is relatively consistent regardless of the fitting window. In terms of the Debye–Waller factor, FDMX predicts a high effective parameter in the XANES region, transitioning to a lower (but also stable) parameter at high energies. This result is readily explainable by the physics of XAFS in the low-energy region, whereby scattering paths from distant neighbour atoms contribute dominantly to the oscillations, resulting in a greater thermal broadening due to decreased vibrational correlations. This allows us to probe the bulk Debye–Waller factor, which we have found to be in excellent agreement with literature values. By contrast, inelastic scattering effects mean that high energy EXAFS is dominated by the contributions from nearest-neighbour atoms, which exhibit a much higher correlation and thus a lower effective thermal parameter σ_{DW}^2. The ability of the FDMX approach to interrogate these features is due entirely to its robust applicability across the entire energy range of XAFS—a result that is achieved without the use of empirical structured spline functions. We plan to extend this work to other data sets including XAFS measurements at multiple temperatures and extract information about static and dynamic disorder.

Acknowledgments

The authors gratefully acknowledge the support of the ARC and ASRP with grants for this work and in particular M Cheah at the ANBF for his time, effort and support in making this work successful.

Appendix A. Sample characterization and tabulated results

A.1. Full foil mapping

Two reference foils with thicknesses of 12.5 μm and 50 μm were mapped with the beam across their entire surface at 23.0731(13) keV in order to measure mass attenuation coefficients on an absolute scale [21]. To ensure that the average spanned the whole foil, measurements of the foil and the perspex holder were also made. With accurate modelling and fitting of the holder to the experimental results, this permits the removal of the holder attenuation and recovers the foils attenuation for the whole sample. Many of the prescriptions used here follow [21], and we compare these results with a simpler model which assumes that the central region of the foil is an accurate representation of the whole foil.

The average attenuation of the foil is directly related to the average integrated column density such that [21]

$$\overline{\left(\left[\frac{\mu}{\rho}\right][\rho t]_{xy}\right)}_F = \left[\frac{\mu}{\rho}\right]\overline{[\rho t]_{xy}} = \left[\frac{\mu}{\rho}\right]\overline{[\rho t]} = \left[\frac{\mu}{\rho}\right]\frac{m}{A}, \quad (A.1)$$

which enables the absolute value of the mass attenuation coefficient to be determined with accurate knowledge of the mass m, the cross sectional area A, and the average attenuation of the foil.

There are three main regions of interest. The first region is simply where only foil measurements were made. No special attention needs to be paid to this area. The second region is any section where the beam only partially interacts with the foil. This requires precise knowledge of the edge of the foil, which is mapped and determined in the fitting procedure. The third section is the region where the beam passed through the holder as well as the foil.

The model uses geometrical shapes for the shape of the beam, foil and holder. The current holder differs from previous holders [21], in that it consists of only two perspex strips along the left and right sides of the foil in order to hold it in place. This improvement means that the x-ray beam interacts with less of the holder, and there is therefore less uncertainty in the procedure for removal of the holder attenuation from the total attenuation. The foil was modelled as a wedge in x and y centred about its geometrical centre. Accurate modelling of the foil is not necessary for the removal of the holder contributions.

The total attenuation profile of the 50 μm foil is presented in figure A1 showing clear structural features such as holder screws, the perspex holder at the left and right edge and the flat central region representing foil only measurements. Once the holder attenuation profile had been removed and the pure foil attenuation recovered, the average foil attenuation was evaluated by

$$\overline{\left(\left[\frac{\mu}{\rho}\right][\rho t]_{xy}\right)}_F = \frac{1}{A}\sum_i a_i\left(\left[\frac{\mu}{\rho}\right][\rho t]_i\right) \quad (A.2)$$

where a_i is the area of the beam hitting the foil, with the property that $\sum_i a_i = A$. Combining this with equation (A.1) and

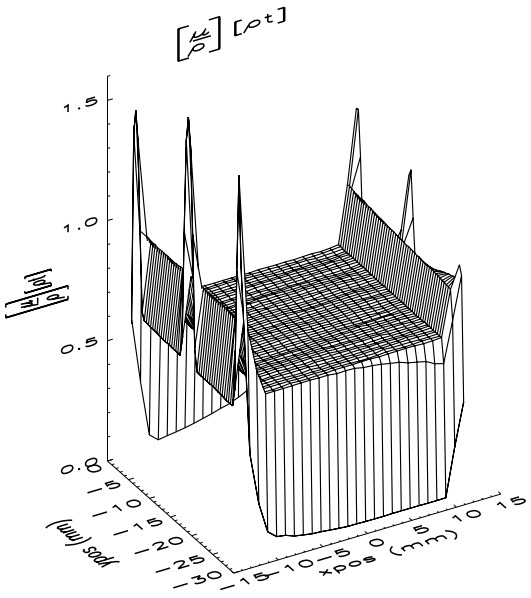

Figure A1. Attenuation profile of the 50 μm foil at 23 keV as a function of its x and y location. Prominent features of the profile include the six large spikes at the left and right edges, corresponding to screws in the holder, the flat section of foil only and the raised left and right edges where the beam passed through foil and perspex.

the accurate determination of A and m, the absolute mass attenuation coefficient is able to be calculated, free of any assumptions about foil non-uniformity.

The mass attenuation coefficient is then calculated from

$$\left[\frac{\mu}{\rho}\right] = \frac{A}{m}\overline{\left[\frac{\mu}{\rho}\right][\rho t]} \quad (A.3)$$

and the final uncertainty in the mass attenuation coefficient is then

$$\frac{\Delta_{[\mu/\rho]}}{[\mu/\rho]} = \sqrt{\left(\frac{\Delta A}{A}\right)^2 + \left(\frac{\Delta m}{m}\right)^2 + \left(\frac{\Delta_{\left[\frac{\mu}{\rho}\right][\rho t]}}{\left[\frac{\mu}{\rho}\right][\rho t]}\right)^2} \quad (A.4)$$

where the uncertainty in $\left[\frac{\mu}{\rho}\right][\rho t]$ comes from the full foil mapping results. The average attenuations determined by each of the two approaches for the 50 μm and 12.5 μm foils are presented in table A1.

The two approaches agree to within around 2 standard deviations for the 50 μm foil. The full foil mapping result has a slightly higher uncertainty than the central map approach, because the outer regions of the foil have higher uncertainty. Fitting uncertainties are scaled by χ_r^2 which provides an overestimate. The model does not intend to describe the structure of the foil. The full foil result remains a better description of the average absorption of the foil than the central only region.

The two approaches agree (only) to within around 5 standard deviations for the 12.5 μm foil. The full foil method aims to encompass all structure of the foil, so in this case the outer regions of the foil appear to differ in thickness from the central region. The full foil method result for this foil

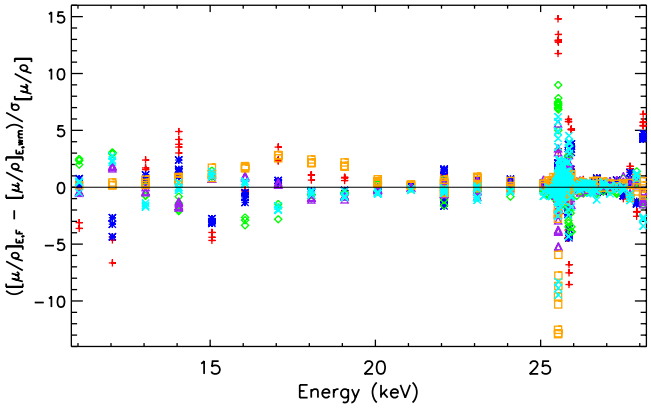

Figure A2. Significance of the deviations from the weighted mean. The markers represent results obtained using foils of varying thickness.

has a slightly lower uncertainty. The discrepancy between the two methods is partially explained by the fact that the model was unable to fully describe certain irregular structure of the 12.5 μm foil and hence the residuals could not be fully accounted for.

The final results of the full foil mapping results found the absolute absorption, $\left[\frac{\mu}{\rho}\right]$ to be 12.242 (cm^2 g^{-1}) $\pm$ 0.036% and 12.224 (cm^2 g^{-1}) $\pm$ 0.03% for the 12.5 μm and 50 μm foil respectively. The difference between the two determined values is 0.018 cm^2 g^{-1} or around 0.14%. This is broadly consistent, but the discrepancy is significant. The absolute value of $\left[\frac{\mu}{\rho}\right]_{\mathrm{abs}}$ was taken to be the value determined for the 50 μm foil.

A.2. Determining the local integrated column densities

Full foil mapping requires significant experimental allocation to obtain the mass attenuation coefficient on an absolute scale, so is only performed on selected foils. In this experiment it was performed on two foils at 23 kev, achieving uncertainties of 0.03%.

As the beam passes through the same point on each foil and every energy, the integrated column density is common for all energies. This is an important feature of the XERT as it permits the calibration of each foil to a single value of the local integrated column density, given that the beam intersection of the sample does not change significantly. Therefore, each foil attenuation is scaled with the fitted parameter $[\rho \mathrm{t}]_F$, where the subscript F denotes the specific foil label. The foils are scaled such that

$$\left[\frac{\mu}{\rho}\right]_F = \frac{\left(\left[\frac{\mu}{\rho}\right][\rho \mathrm{t}]\right)_{\mathrm{meas}}}{[\rho \mathrm{t}]_F}, \tag{A.5}$$

Table A1. Results from both methods used to determine the absolute value of the mass attenuation coefficient.

t_{nom} (μm)	$\left[\frac{\mu}{\rho}\right][\rho \mathrm{t}]_c$	$\left[\frac{\mu}{\rho}\right][\rho \mathrm{t}]_f$	$\Delta_{\left[\frac{\mu}{\rho}\right][\rho \mathrm{t}]_c}$ (%)	$\Delta_{\left[\frac{\mu}{\rho}\right][\rho \mathrm{t}]_f}$ (%)
12.5	0.16223	0.16206	0.027%	0.021%
50	0.64979	0.64962	0.0091%	0.011%

The subscripts c and f represent the central and full regions respectively used in the calculation.

The appearance of the integrated column density twice in equation (A.5) should not be confusing, as we measure $[\mu/\rho][\rho \mathrm{t}]_{\mathrm{meas}}$ and fit the parameter $[\rho \mathrm{t}]_F$ independently [18]. To enforce local consistency between results made with different foils and the full foil mapping result, the integrated column densities are fitted with the implementation of a Levenberg–Marquardt algorithm to minimise

$$\chi^2 = \sum_{E_i} \sum_{F_j} \left(\frac{\left[\frac{\mu}{\rho}\right]_{E_i F_j} - \overline{\left[\frac{\mu}{\rho}\right]_{E_i}}}{\sigma_{\left[\frac{\mu}{\rho}\right]_{E_i F_j}}} \right)^2, \tag{A.6}$$

where $[\mu/\rho]_{E_i F_j}$ is the mass attenuation coefficient of foil F_j at energy E_i with the associated uncertainty $\sigma_{[\mu/\rho]_{E_i F_j}}$ and $\overline{[\mu/\rho]}_{E_i}$ is the weighted mean of all foils and aperture conditions at energy E_i. Minimisation of χ^2 ensures that the results of all foils are consistent with the full foil mapping measurements and deviations are minimised between foils at each energy. The integrated column density of an individual foil is not directly measured, rather the scaling of the parameter is relative to results of all foils. Use of $\chi_r^2 = \chi^2/(N_f - N_p)$, where N_f is the number of degrees of freedom or data points with N_p is the number of parameters, allows the inclusion of additional parameters to be scrutinised.

The initial estimates of the local integrated column density yielded a large χ_r^2 of 7.97. While this indicates a decent starting point, there are likely uncorrected systematic errors causing deviations between foils of different thickness.

Further analysis of these deviations following de Jonge's prescription of presenting the significance of deviations [22] show clear discrepancies around the absorption edge as shown in figure A2. Since the significance of most deviations is less than around 2, and generally no greater that 5, the deviations around the absorption edge reveal the presence of a systematic error.

Inspection of this region provides evidence that there is a systematic shift along the absorption edge. Our group has previously reported measurements of the systematic shift caused by bandwidth [33], which we further investigate in section 4.

A.3. Tabulated mass attenuation coefficients and form factors

Table A2. Mass attenuation coefficients $\left[\frac{\mu}{\rho}\right]$ and the imaginary component of the atomic form-factor f_2 as a function of x-ray energy, with one standard deviation uncertainties in the least significant digits indicated in parentheses.

E (keV)	$\left[\frac{\mu}{\rho}\right]$ (cm^2 g^{-1})	$(\Delta_{[\mu/\rho]})_r$ (%)	$(\Delta_{[\mu/\rho]})_a$ (%)	$\left[\frac{\mu}{\rho}\right]_{R+C}$ (cm^2 g^{-1})	$\left[\frac{\mu}{\rho}\right]_{pe}$ (cm^2 g^{-1})	f_2 (*e*/atom)
11.03599 (46)	92.743 (32)	0.01%	0.03%	2.417 (18)	90.33 (68)	2.555 (19)
12.04001 (47)	73.124 (54)	0.06%	0.07%	2.2126 (61)	70.91 (20)	2.1886 (63)
13.04339 (51)	58.876 (31)	0.04%	0.05%	2.0352 (30)	56.841 (89)	1.9005 (30)
14.04618 (56)	47.995 (29)	0.05%	0.06%	1.8788 (88)	46.12 (22)	1.6604 (78)
15.04851 (63)	39.761 (33)	0.07%	0.08%	1.740 (12)	38.02 (27)	1.467 (11)
16.05173 (70)	33.312 (13)	0.02%	0.03%	1.617 (14)	31.70 (28)	1.304 (12)
17.05414 (79)	28.163 (14)	0.03%	0.04%	1.507 (15)	26.66 (26)	1.165 (11)
18.05675 (87)	24.0872 (81)	0.01%	0.03%	1.408 (15)	22.68 (24)	1.050 (11)
19.06100 (96)	20.7471 (69)	0.01%	0.03%	1.319 (14)	19.43 (21)	0.949 (10)
20.0634 (11)	18.0557 (67)	0.02%	0.03%	1.239 (13)	16.82 (18)	0.8649 (92)
21.0676 (12)	15.6542 (62)	0.02%	0.03%	1.166 (12)	14.49 (15)	0.7824 (81)
22.0699 (13)	13.8502 (92)	0.05%	0.06%	1.101 (11)	12.75 (13)	0.7213 (74)
23.0731 (13)	12.2237 (48)	0.02%	0.03%	1.042 (10)	11.18 (11)	0.6614 (66)
24.0772 (14)	10.8552 (55)	0.04%	0.05%	0.9874 (97)	9.868 (97)	0.6090 (60)
25.0775 (15)	9.6768 (50)	0.04%	0.05%	0.9384 (93)	8.738 (86)	0.5617 (56)
25.2267 (16)	9.5448 (46)	0.03%	0.04%	0.9315 (92)	8.613 (86)	0.5570 (55)
25.3269 (16)	9.4963 (44)	0.03%	0.04%	0.9269 (92)	8.569 (85)	0.5564 (55)
25.3757 (16)	9.5290 (47)	0.03%	0.04%	0.9246 (92)	8.604 (86)	0.5597 (56)
25.4262 (16)	9.6595 (48)	0.03%	0.04%	0.9223 (92)	8.737 (87)	0.5695 (57)
25.4468 (16)	9.7641 (44)	0.03%	0.04%	0.9214 (92)	8.843 (88)	0.5768 (58)
25.4659 (16)	10.0110 (66)	0.05%	0.06%	0.9206 (92)	9.090 (91)	0.5934 (59)
25.4760 (16)	10.2158 (44)	0.03%	0.04%	0.9201 (92)	9.296 (93)	0.6071 (61)
25.4854 (16)	10.5658 (54)	0.04%	0.05%	0.9197 (92)	9.646 (96)	0.6302 (63)
25.4948 (16)	11.1115 (62)	0.04%	0.05%	0.9192 (92)	10.19 (10)	0.6661 (67)
25.5002 (16)	11.7262 (76)	0.05%	0.06%	0.9190 (92)	10.81 (11)	0.7064 (71)
25.5052 (16)	12.6870 (92)	0.06%	0.07%	0.9187 (91)	11.77 (12)	0.7694 (77)
25.5102 (16)	15.392 (36)	0.23%	0.23%	0.9184 (91)	14.47 (15)	0.9464 (96)
25.5150 (16)	21.829 (68)	0.30%	0.31%	0.9182 (91)	20.91 (22)	1.368 (14)
25.5197 (16)	34.01 (12)	0.36%	0.36%	0.9180 (91)	33.10 (35)	2.165 (23)
25.5244 (16)	46.38 (16)	0.34%	0.34%	0.9178 (91)	45.47 (48)	2.975 (31)
25.5298 (16)	55.213 (62)	0.10%	0.11%	0.9176 (91)	54.30 (54)	3.553 (35)
25.5351 (16)	57.552 (37)	0.05%	0.06%	0.9173 (91)	56.63 (56)	3.707 (37)
25.5399 (16)	55.817 (47)	0.07%	0.08%	0.9171 (91)	54.90 (54)	3.594 (36)
25.5449 (16)	56.432 (52)	0.08%	0.09%	0.9169 (91)	55.51 (55)	3.635 (36)
25.5508 (16)	60.625 (54)	0.08%	0.08%	0.9166 (91)	59.71 (59)	3.911 (39)
25.5559 (16)	61.568 (61)	0.09%	0.09%	0.9164 (91)	60.65 (60)	3.973 (39)
25.5615 (16)	57.879 (46)	0.07%	0.07%	0.9161 (91)	56.96 (56)	3.732 (37)
25.5666 (16)	55.877 (36)	0.05%	0.06%	0.9159 (91)	54.96 (54)	3.602 (36)
25.5767 (16)	59.030 (67)	0.11%	0.11%	0.9155 (91)	58.11 (58)	3.810 (38)
25.5868 (16)	62.475 (44)	0.06%	0.06%	0.9150 (91)	61.56 (61)	4.038 (40)
25.5969 (16)	58.847 (61)	0.10%	0.10%	0.9146 (91)	57.93 (58)	3.801 (38)
25.6068 (16)	57.402 (37)	0.05%	0.06%	0.9141 (91)	56.49 (56)	3.708 (37)
25.6163 (16)	59.234 (33)	0.04%	0.05%	0.9137 (91)	58.32 (58)	3.830 (38)
25.6262 (16)	60.492 (43)	0.06%	0.07%	0.9133 (91)	59.58 (59)	3.914 (39)
25.6357 (16)	60.048 (41)	0.06%	0.06%	0.9128 (91)	59.14 (59)	3.886 (39)
25.6456 (16)	58.714 (39)	0.05%	0.06%	0.9124 (91)	57.80 (57)	3.800 (38)
25.6557 (16)	58.626 (45)	0.07%	0.07%	0.9120 (91)	57.71 (57)	3.796 (38)
25.6653 (16)	59.650 (38)	0.05%	0.06%	0.9115 (91)	58.74 (58)	3.864 (38)
25.6752 (16)	59.631 (43)	0.06%	0.07%	0.9111 (91)	58.72 (59)	3.865 (39)
25.6860 (16)	59.027 (38)	0.05%	0.06%	0.9106 (91)	58.12 (58)	3.827 (38)
25.6959 (16)	58.484 (33)	0.04%	0.05%	0.9102 (91)	57.57 (57)	3.792 (38)
25.7064 (16)	58.133 (38)	0.05%	0.06%	0.9097 (91)	57.22 (57)	3.771 (38)

(*Continued*)

Table A2. (*Continued*)

E (keV)	$\left[\frac{\mu}{\rho}\right]$ (cm^2 g^{-1})	$(\Delta_{[\mu/\rho]})_r$ (%)	$(\Delta_{[\mu/\rho]})_a$ (%)	$\left[\frac{\mu}{\rho}\right]_{R+C}$ (cm^2 g^{-1})	$\left[\frac{\mu}{\rho}\right]_{pe}$ (cm^2 g^{-1})	f_2 (*e*/atom)
25.7173 (16)	58.175 (51)	0.08%	0.08%	0.9092 (91)	57.27 (57)	3.775 (38)
25.7272 (16)	58.819 (48)	0.07%	0.08%	0.9088 (91)	57.91 (58)	3.819 (38)
25.7425 (16)	58.872 (33)	0.04%	0.05%	0.9081 (91)	57.96 (58)	3.825 (38)
25.7570 (16)	57.794 (48)	0.07%	0.08%	0.9075 (91)	56.89 (57)	3.756 (38)
25.7718 (16)	57.114 (26)	0.03%	0.04%	0.9068 (91)	56.21 (56)	3.713 (37)
25.7860 (16)	57.248 (47)	0.07%	0.08%	0.9062 (91)	56.34 (56)	3.724 (37)
25.8008 (16)	57.765 (39)	0.05%	0.06%	0.9056 (91)	56.86 (57)	3.761 (38)
25.8157 (16)	57.61 (13)	0.22%	0.22%	0.9049 (91)	56.70 (58)	3.752 (38)
25.8312 (16)	57.02 (19)	0.33%	0.33%	0.9043 (91)	56.11 (59)	3.715 (39)
25.8463 (16)	56.44 (23)	0.40%	0.40%	0.9036 (91)	55.54 (60)	3.680 (40)
25.8624 (16)	56.846 (86)	0.14%	0.15%	0.9029 (91)	55.94 (57)	3.709 (38)
25.8780 (16)	56.460 (39)	0.06%	0.06%	0.9022 (91)	55.56 (56)	3.685 (37)
25.8984 (16)	56.681 (67)	0.11%	0.11%	0.9013 (91)	55.78 (56)	3.703 (37)
25.9179 (16)	56.59 (21)	0.36%	0.36%	0.9005 (91)	55.69 (60)	3.700 (40)
26.0812 (16)	54.967 (52)	0.08%	0.09%	0.8935 (90)	54.07 (55)	3.615 (37)
26.1819 (17)	54.253 (48)	0.08%	0.08%	0.8892 (90)	53.36 (54)	3.582 (36)
26.2811 (17)	53.737 (48)	0.08%	0.08%	0.8850 (90)	52.85 (54)	3.561 (36)
26.3830 (17)	53.098 (35)	0.05%	0.06%	0.8807 (90)	52.22 (53)	3.531 (36)
26.4831 (17)	52.421 (44)	0.07%	0.08%	0.8765 (90)	51.54 (53)	3.499 (36)
26.5831 (17)	51.852 (39)	0.06%	0.07%	0.8724 (90)	50.98 (52)	3.474 (36)
26.6877 (17)	51.33 (10)	0.19%	0.19%	0.8682 (89)	50.46 (53)	3.452 (36)
26.8872 (17)	50.100 (49)	0.09%	0.09%	0.8601 (89)	49.24 (51)	3.394 (35)
27.0872 (17)	49.024 (52)	0.10%	0.10%	0.8522 (89)	48.17 (51)	3.345 (35)
27.2884 (18)	47.887 (64)	0.12%	0.13%	0.8444 (89)	47.04 (50)	3.291 (35)
27.4910 (18)	46.88 (11)	0.23%	0.24%	0.8367 (89)	46.04 (50)	3.244 (36)
27.6921 (18)	45.94 (18)	0.39%	0.39%	0.8291 (89)	45.11 (52)	3.202 (37)
27.8919 (18)	44.93 (24)	0.53%	0.53%	0.8217 (89)	44.11 (53)	3.154 (38)
28.0903 (19)	44.04 (47)	1.07%	1.07%	0.8145 (89)	43.22 (66)	3.112 (48)

We present also the relative and absolute percentage uncertainty in the mass attenuation coefficients, $(\Delta_{[\mu/\rho]})_r$ and $(\Delta_{[\mu/\rho]})_a$ respectively. Uncertainty in $\left[\frac{\mu}{\rho}\right]_{pe}$ and f_2 includes the measurement uncertainty and the difference between major tabulations of the total Rayleigh plus Compton scattering cross-sections. Values of f_2 in the XAFS region are affected by solid state effects.

References

[1] Rehr J J and Albers R C 2000 *Rev. Mod. Phys.* **72** 621
[2] Richwin M, Zaeper R, Lutzenkirchen-Hect D and Frahm R 2001 *J. Synchrotron Radiat.* **8** 354
[3] Brugger J, Etschmann B, Liu W, Testemale D, Hazemann J, Emerich H, van Beek W and Proux O 2007 *Geochim. Cosmochim. Acta* **71** 4920
[4] Pettifer R F, Borowski M and Loeffen P W 1999 *J. Synchrotron Radiat.* **6** 217
[5] Chantler C T 2009 *Eur. Phys. J. Spec. Top.* **169** 147
[6] Pratt R 2014 *Rad. Phys. Chem.* **95** 4
[7] Sayers D E, Lytle F W and Stern E A 1971 *Adv. X-Ray Anal.* **13** 248
[8] Joly Y 2001 *Phys. Rev.* B **63** 125120
[9] Bourke J D, Chantler C T and Witte C 2007 *Phys. Lett.* A **360** 702
[10] Chantler C T, Barnea Z, Tran C Q, Tiller J B and Paterson D 1999 *Opt. Quantum Electron.* **31** 495
[11] Chantler C T and Bourke J D 2010 *J. Phys. Chem. Lett.* **1** 2422
[12] Bourke J D and Chantler C T 2010 *Phys. Rev. Lett.* **104** 206601
[13] Chantler C T, Tran C Q, Paterson D, Barnea Z and Cookson D J 2000 *X-Ray Spectrom.* **29** 449
[14] Chantler C T, Tran C Q, Paterson D, Cookson D J and Barnea Z 2000 *X-Ray Spectrom.* **29** 459
[15] Nordfors B 1960 *Ark. Fys.* **18** 37
[16] Creagh D and Hubbell J 1987 *Acta Cryst.* **43** 102
[17] Creagh D C 1999 *X-ray absorption spectra, in International Tables for Crystallography* 2nd edn vol C ed A J C Wilson (Boston: Kluwer)
[18] Chantler C T, Barnea Z, Tran C Q, Rae N A and de Jonge M D 2012 *J. Synchrotron Radiat.* **19** 851
[19] Tran C Q, Chantler C T, Barnea Z, de Jonge M D, Dhal B B, Chung C, Paterson D, Lee P, Wang J and Cookson D J 2005 *J. Phys.* B **38** 89
[20] de Rooij A 1989 *ESA J.* **13** 363
[21] de Jonge M D, Barnea Z, Tran C Q and Chantler C T 2004 *Meas. Sci. Technol.* **15** 1811
[22] de Jonge M D, Tran C Q, Chantler C T, Barnea Z, Dhal B B, Cookson D J, Lee W and Mashayekhi A 2005 *Phys. Rev.* A **71** 032702
[23] Rae N A, Chantler C T, Tran C Q and Barnea Z 2006 *Rad. Phys. Chem.* **75** 2063
[24] Tantau L J, Islam M T, Payne A T, Tran C Q, Cheah M H, Best S P and Chantler C T 2013 *Rad. Phys. Chem.* **95** 73
[25] Chantler C T, Tran C Q and Cookson D J 2004 *Phys. Rev.* A **69** 042101

[26] Chantler C T, Rae N A and Tran C Q 2007 *J. Appl. Cryst.* **40** 232
[27] Tran C Q, de Jonge M D, Barnea Z and Chantler C T 2004 *J. Phys.* B **37** 3163
[28] Rae N A, Chantler C T, Barnea Z, de Jonge M D, Tran C Q and Hester J R 2010 *Phys. Rev.* A **81** 022904
[29] Barnea Z, Chantler C T, Glover J L, Grigg M W, Islam M T, de Jonge M D, Rae N A and Tran C Q 2011 *J. Appl. Cryst.* **44** 281
[30] Tran C Q, Barnea Z, de Jonge M D, Dhal B B, Paterson D, Cookson D J and Chantler C T 2003 *X-Ray Spectrom.* **32** 69
[31] Glover J L and Chantler C T 2009 *X-Ray Spectrom.* **38** 510
[32] Glover J L, Chantler C T and de Jonge M D 2009 *Phys. Lett.* A **373** 1177
[33] de Jonge M D, Barnea Z, Tran C Q and Chantler C T 2004 *Phys. Rev.* A **69** 022717
[34] Islam M T, Tantau L J, Rae N A, Barnea Z, Tran C Q and Chantler C T 2014 *J. Synchrotron Radiat.* **21** 413
[35] Barnea Z, Creagh D, Davis T, Garrett R, Janky S, Stevenson A and Wilkins S 1992 *Rev. Sci. Instrum.* **63** 1069
[36] Barnea Z *et al* 1989 *Rev. Sci. Instrum.* **60** 2537
[37] Sandiago, Umesh T K and Gowda R 1997 *Pramana J. Phys* **48** 1077
[38] Tajuddin A, Chong C, Shukri A, Bandyopadhyay T and Bradley D 1995 *Appl. Radiat. Isot.* **46** 113
[39] Chantler C T 2000 *J. Phys. Chem. Ref. Data* **29** 597
[40] Chantler C T 1995 *J. Phys. Chem. Ref. Data* **24** 71
[41] Chantler C T, Olsen K, Dragoset R A, Kishore A R, Kotochigova S A and Zucker D S 2003 *X-Ray Form Factor, Attenuation and Scattering Tables (version 2.0)* (Gaithersburg, MD: National Institute of Standards and Technology) [Online] Available: http://physics.nist.gov/ffast
[42] Berger M J and Hubbell J H 2004 *NIST Stand. Ref. Database 8* **87** 3597
[43] Dreier P, Rabe P, Malzfeldt P and Neimann W 1984 *J. Phys.* C **17** 3123
[44] Creagh D 1987 *Nucl. Instrum. Methods* A **255** 1
[45] Creagh D 1989 *Nucl. Instrum. Methods* A **280** 180
[46] Creagh D 1991 *Chin. J. Phys.* **29** 299
[47] de Jonge M D *et al* 2007 *Phys. Rev.* A **75** 32702
[48] Glover J L, Chantler C T, Barnea Z, Rae N A and Tran C Q 2010 *J. Phys.* B **43** 085001
[49] Smale L F, Chantler C T, de Jonge M D, Barnea Z and Tran C Q 2006 *Radiat. Phys. Chem.* **75** 1559
[50] Chantler C T and Bourke J D 2014 *J. Phys.: Condens. Matter* **26** 145401
[51] Joly Y, Cabaret D, Renevier H and Natoli C 1999 *Phys. Rev. Lett.* **82** 2398
[52] Rehr J J, Kas J J, Prange M P, Sorini A P, Takimoto Y and Vila F D 2009 *C. R. Phys.* **10** 548
[53] Liu L and Bassett W A 1973 *J. Appl. Phys.* **44** 1475
[54] Butt N M, Bashir J, Willis B T M and Heger G 1988 *Acta. Cryst.* A44 396
[55] Alexopoulos K, Boskovits J, Mourikis S and Roilos M 1965 *Acta. Cryst.* **19** 349
[56] Linkoaho M V 1971 *Phil. Mag.* **23** 191
[57] Kashiwase Y 1979 *Japan. J. Appl. Phys.* **18** 657
[58] Pathak P D and Shah N P 1979 *Indian J. Pure Appl. Phys.* A **53** 283
[59] Vega H, Forsterling G and Kleinstuck K 1980 *Krist. Tech.* **15** 815
[60] Willis B T M and Pryor A W 1975 *Thermal Vibrations in Crystallography* (Cambridge: Cambridge University Press)
[61] Cosgriff E C, Chantler C T, Witte C, Smale L F and Tran C Q 2005 *Phys. Lett.* A **343** 174
[62] Bourke J D and Chantler C T 2010 *Nucl. Instrum. Methods* A **619** 33
[63] Krause M O and Oliver J H 1979 *J. Phys. Chem. Ref. Data* **8** 329
[64] Tanuma S, Powell C J and Penn D R 2011 *Surf. Interface Anal.* **43** 689
[65] Blaha P, Schwarz K, Madsen G K H, Kvasnicka D and Luitz J 2001 *An Augmented Plane Wave Plus Local Orbitals Program for Calculating Crystal Properties* (Austria: Vienna University of Technology)
[66] Ambrosch-Draxl C and Sofo J O 2006 *Comput. Phys. Commun.* **175** 1
[67] Williams G I and Owen E A 1954 *J. Sci. Instrum.* **31** 49
[68] Wyckoff R W G 1963 *Crystal Structures* 2nd edn (New York: Interscience Publishers)
[69] Dubiel M, Brunsch S and Troger L 2001 *J. Synchrotron Radiat.* **8** 539
[70] Vila F D, Rehr J, Rossner H and Krappe H 2007 *Phys. Rev.* B **76** 014301
[71] Rehr J J and Albers R C 1990 *Phys. Rev.* B **41** 8139
[72] Stern E A, Bunker B A and Heald S M 1980 *J. Synchrotron Radiat.* **21** 5521
[73] Dalba G and Fornasini P 1997 *J. Synchrotron Radiat.* **4** 243
[74] Garino C, Borfecchia E, Gobetto R, van Bokhoven J A and Lamberti C 2014 *Coord. Chem. Rev.* 277–8 130
[75] Smolentsev G and Soldatov A V 2007 *Comput. Mater. Sci.* **39** 569
[76] Glover J L, Chantler C T, Soldatov A V, Smolentsev G and Feiters M C 2007 *AIP Conf. Proc.* **882** 625